



CFD studies on the separation performance of a new combined gas–solid separator used in TMSR-SF

Mengdan Wu¹ · Ning Zhang² · Jinguo Zhai³ · Guo-Yan Zhou¹ · Shan-Tung Tu¹

Received: 14 December 2018 / Revised: 6 May 2019 / Accepted: 14 May 2019 / Published online: 12 August 2019

© China Science Publishing & Media Ltd. (Science Press), Shanghai Institute of Applied Physics, the Chinese Academy of Sciences, Chinese Nuclear Society and Springer Nature Singapore Pte Ltd. 2019

Abstract In order to comply with discharge standards, a gas–solid separator is used to remove solid particles from the thorium molten salt reactor-solid fuel (TMSR-SF) system. As a key component, it directly determines system energy efficiency. However, current gas–solid separators, based on activated carbon adsorption technology, result in high pressure drops and increased maintenance costs. In the present study, a new combined gas–solid separator was developed for the TMSR-SF. Based on a simplified computational fluid dynamics (CFD) model, the gas–solid two-phase flow and the motion trajectory of solid particles were simulated for this new separator using commercial ANSYS 16.0 software. The flow and separation mechanism for this structure were also been discussed in terms of their velocity effects and pressure field distributions, and then the structure was optimized based on the influence of key structural parameters on pressure and separation efficiency. The results showed that the standard k – ϵ model could be achieved and accurately simulated the new combined separator. In this new combined gas–solid separator, coarse particles are separated in the first stage using

rotating centrifugal motion, and then fine particles are filtered in the second stage, giving a separation efficiency of up to 96.11%. The optimum blade inclination angle and numbers were calculated to be 45° and four, respectively. It implicated that the combined separator could be of great significance in a wide variety of applications.

Keywords Combined separator · Gas–solid two-phase flow · Structure optimization · CFD · TMSR-SF

1 Introduction

The molten salt reactor (MSR) is a generation IV reactor that shows promise in terms of its ability to satisfy increasing electricity demands. Due to its many remarkable advantages—being safe, economic, and applying sustainable development of fissile resources and nuclear non-proliferation [1]—it has attracted interest from various researchers [2, 3]. The thorium-based molten salt reactor (TMSR) has become increasingly prominent, based on its excellent breeding capability in both thermal and fast spectrum reactors, and less long-lived minor actinides resulting from fission and due to the abundance of thorium reserves that are available [4]. The fluoride-salt-cooled-high-temperature reactor (FHR), which is basically an MSR with solid fuel, can deliver heat at high temperatures—above 600 °C—and exhibits attractive economic performance while achieving outstanding safety and security standards [5–8]. In order to verify the technical feasibility and practicality of large-scale thorium-based FHRs, the Shanghai Institute of Applied Physics (SIAP) initiated a pioneering Molten Salt Reactor Experiment (MSRE) research program that involved designing and planning the

✉ Guo-Yan Zhou
zhougy@ecust.edu.cn

✉ Shan-Tung Tu
sttu@ecust.edu.cn

¹ Key Laboratory of Pressure Systems and Safety (MOE), School of Mechanical and Power Engineering, East China University of Science and Technology, Shanghai 200237, China

² Shanghai Institute of Applied Physics, Chinese Academy of Sciences, Shanghai 201800, China

³ Shanghai Research Institute of Chemical Industry, Shanghai 200062, China

construction of a 2 MWth Th-U pebble-bed TMSR-SF with Solid Fuel in 2020 [9–12]. In this nuclear system (as shown in Fig. 1), the process gas will be cooled to < 100 °C after reaction, in the aerosol condenser, in preparation for release. However, the high-temperature salt spray, which includes beryllium, lithium, uranium, and other radioactive materials, will escape with the argon gas, and will be condensed into solid particles of 0.03–10 μm in diameter. Direct emission of this nuclear waste gas will cause environmental pollution, indicating that a high-efficiency exhaust removal system is needed, and will form basic emission control equipment in future TMSR-SF reactor designs.

At present, gas–solid separation equipment that is based on activated carbon adsorption technology is the most popular cleaning equipment in nuclear power systems [13]. Due to particle wear, the activated carbon is easily damaged and needs frequent replacement—which causes high pressure drop and considerable economic loss [14]. Mechanical separation equipment, however, such as a cyclone, has not only good wear resistance, but also has a simple structure, with the added advantages of low cost and convenient maintenance [15]. Its disadvantage is that it has high separation efficiency only for particles > 5 μm [16]; thus, one or more separators need to be added in series to separate particles < 5 μm , which consumes more materials and floor space, involves complicated structures, and reduces low efficiency.

These issues show that separation equipment with a compact structure, with high efficiency, operating with a low pressure drop, and exhibiting a long service life, is urgently needed for the next-generation nuclear system TMSR-SF. Considering the advantages of both filters and

axial cyclone separators, a novel combined separator has been proposed [17], for application to TMSR-SF technology, as shown in Fig. 2. In order to optimize design and to manufacture this new equipment, its internal flow field and separation performance have required further study.

Many numerical studies have been performed on filters and cyclone separators. Tronville and Sala [18] and Hu et al. [19] modeled the influence of filter structure on a flow field and identified an optimal filter structure size. Zhou and Soo [20] and Tian et al. [21] used the standard k – ϵ model and Reynolds Stress model to simulate the separator and compared it with measured results to verify the feasibility of a numerical simulation method. Azadi et al. [22] simulated gas particulate flow inside different-sized cyclones, while Nor et al. [23] and Wasilewski [24] numerically studied the influence of cyclone separator structure on flow field performance. All these studies were conducted for a single filter or separator, while there have been few studies on the flow field of a setup like the new combined separator. Therefore, a feasible and accurate numerical model or method is necessary, in order to study the separation performance of this combined separator. It is also important in terms of design optimization and to facilitate wide application of this new separator that its separation mechanism and the influence of structural parameters on pressure drop and separation efficiency are clarified.

In this study, a numerical model of the new combined separator has been established. Based on the optimum turbulence model, the gas-phase flow field and the gas–solid two-phase flow field have been numerically simulated, using the commercial ANSYS 16.0 software. The pressure drop and gas–solid separation performance were

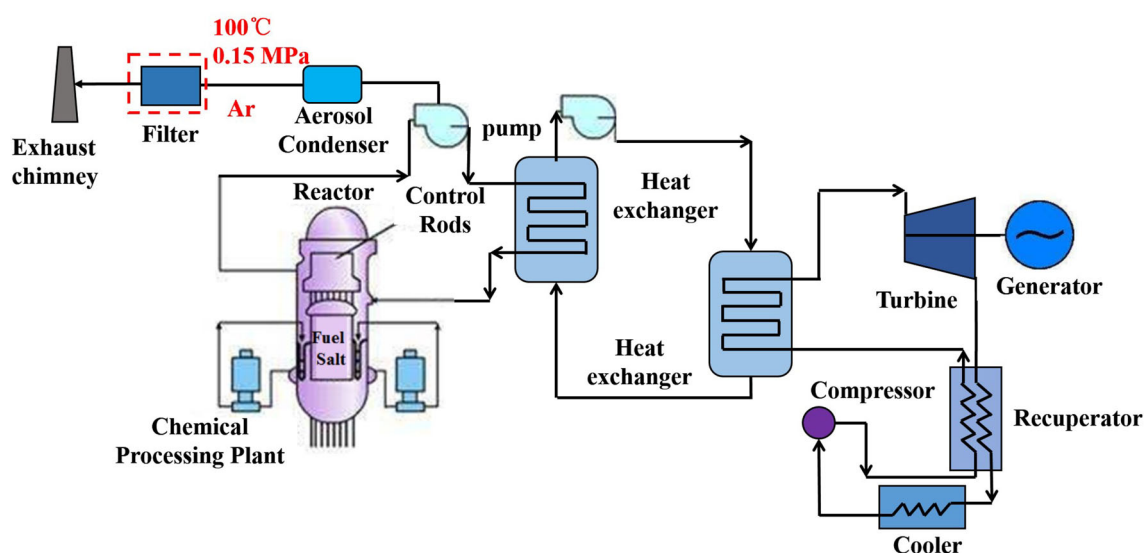


Fig. 1 (Color online) Schematic diagram of TMSR

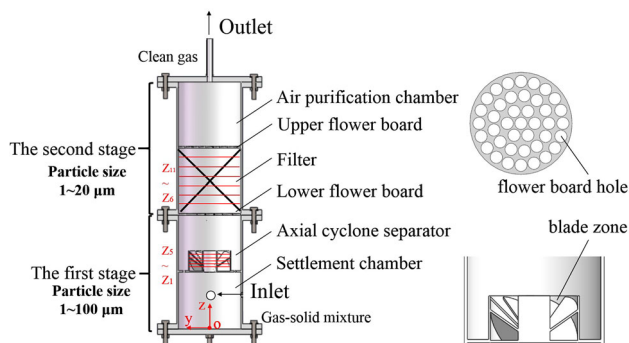


Fig. 2 Proposed combined separator structure

studied further by systematically examining the influence of structural parameters on separation performance. Finally, an optimized blade structure—the key component of the combined separator—was identified.

2 Geometric model

The new separator is compact and consists of two stages, as shown in Fig. 2. The first stage includes a settlement chamber and an axial blade cyclone separator, and is mainly used for the inertial separation of large particles. The second stage consists mainly of a filter and an air purification chamber, for capturing very small particles. The complete separator is 0.08 m in diameter and 0.325 m high. The axial blade cyclone separator is 0.15 m high, and consists of six blades at a 60° angle of inclination. The diameter of the blade structure is 0.045 m. The filter is 0.175 m high and consists of two flower boards, with 22 and 43 holes, respectively.

3 Numerical methods

3.1 Mathematical model

3.1.1 Governing equations

Based on the Boussinesq hypothesis, Reynolds-averaged Navier–Stokes equations were solved to predict the continuous phase. For steady and incompressible fluid flow in the separator, ignoring mass forces, the equations are described as shown in (1) and (2) [25]:

Mass conservation equation:

$$\frac{\partial u_i}{\partial x_i} = 0. \tag{1}$$

Momentum conservation equation:

$$\rho u_j \frac{\partial u_i}{\partial x_j} = -\frac{\partial p}{\partial x_i} + \frac{\partial}{\partial x_j} \left[\mu \left(\frac{\partial u_i}{\partial x_j} + \frac{\partial u_j}{\partial x_i} \right) \right] + \frac{\partial \tau_{ij}}{\partial x_j}. \tag{2}$$

In (1) and (2), u , p , ρ , and μ represent the carrying fluid velocity, pressure, density, and viscosity, respectively, and

$$\tau_{ij} = -\overline{\rho u'_i u'_j} \tag{3}$$

is defined as the Reynolds stress tensor, which represents the effects of turbulent fluctuations on fluid flow.

When modeling a confined swirling flow, an accurate description of the flow’s turbulence is important. A number of turbulence models are available, such as the standard k – ϵ model, the RNG k – ϵ model, the realizable k – ϵ model, and the Reynolds stress model (RSM). In this study, the standard k – ϵ model was used to simulate turbulence transport effects. The turbulence kinetic energy k and its rate of dissipation ϵ were obtained from transport Eqs. (4) and (5) [26].

$$\rho \frac{\partial k}{\partial t} + \rho \frac{\partial (u_i k)}{\partial x_i} = \frac{\partial}{\partial x_j} \left[\left(\mu + \frac{\mu_T}{\sigma_k} \right) \frac{\partial k}{\partial x_j} \right] + G_k - \rho \epsilon - Y_M, \tag{4}$$

$$\rho \frac{\partial \epsilon}{\partial t} + \rho \frac{\partial (u_i \epsilon)}{\partial x_i} = \frac{\partial}{\partial x_j} \left[\left(\mu + \frac{\mu_T}{\sigma_\epsilon} \right) \frac{\partial \epsilon}{\partial x_j} \right] + C_{1\epsilon} \frac{\epsilon}{k} G_k - C_{2\epsilon} \rho \frac{\epsilon^2}{k}. \tag{5}$$

In Eqs. (4) and (5), G_k represents the generation of turbulence kinetic energy, and is defined as shown:

$$G_k = 2\mu_T S_{ij} S_{ij}.$$

S_{ij} is defined as

$$S_{ij} = \frac{1}{2} \left(\frac{\partial u_i}{\partial x_j} + \frac{\partial u_j}{\partial x_i} \right).$$

Y_M is included in the k equation to account for compressibility effects in k – ϵ models, and the turbulent viscosity μ_T is computed by combining k and ϵ as follows:

$$\mu_T = \rho C_\mu \frac{k^2}{\epsilon}.$$

The model constants were $C_{1\epsilon} = 1.44$, $C_{2\epsilon} = 1.92$, $C_\mu = 0.09$, $\sigma_k = 1.0$, and $\sigma_\epsilon = 1.3$.

3.1.2 Porous medium model

According to filtration theory, the porous medium model uses an empirical formula to define flow resistance in porous media. S_i is included in the momentum equation, to represent the resistance of a porous medium to fluids, and for simple homogeneous porous media, it is defined as shown in Eq. (6) [27]:

$$S_i = -\left(\frac{\mu}{\alpha} v_i + C_2 \frac{1}{2} \rho |v| v_i\right) \quad (i = x, y, z). \tag{6}$$

When calculating the porous media model, the viscosity resistance coefficient K ($1/\alpha$) and the inertia resistance coefficient C_2 also need to be set.

3.1.3 Gas–solid two-phase flow model

In this study, beryllium (Be) was selected for the particle phase in the gas–solid, two-phase flow. The particle-phase volume fraction was $< 10\%$, and in the discrete phase model (DPM) used to calculate the trajectories of particles in flow, it was assumed that particle–particle interactions were negligible and that they did not affect the flow field. The force balance equation for particle movement in a Lagrangian reference frame is shown in (7)–(10) [28].

$$\frac{du_p}{dt} = F_D(u_A - u_p)_x, \tag{7}$$

$$F_D = \frac{18\mu_A C_D Re_P}{\rho_p d_p^2 24}, \tag{8}$$

$$C_D = C_1 + \frac{C_2}{Re_P} + \frac{C_3}{Re_P}, \tag{9}$$

$$Re_P = \frac{\rho_A d_p |u_p - u_A|}{\mu_A}. \tag{10}$$

In Eqs. (7)–(10), u_A , μ_A , and ρ_A represent the argon velocity, viscosity, and density, respectively, u_p , ρ_p , and d_p represent particulate velocity, density, and diameter, respectively; Re_P is the relative Reynolds number, C_D is the drag coefficient, and C_1 to C_3 are constants that depend on the range of Re_P [29].

3.2 Boundary conditions

3.2.1 Gas-phase flow field

The fluid medium was argon, with a pressure of 0.15 MPa, and temperature of 100 °C; the density, ρ , was 1.93 kg/m³, and viscosity, μ , was 2.745×10^{-5} Pa s. Boundary conditions at each zone were as follows:

1. Inlet: Inlet velocity. The velocity at inlet v_{in} was 50 m/s, and it was assumed that the entrance turbulence was well-developed and was scattered evenly across the entire inlet cross section. At the same time, entrance turbulence was determined by setting turbulence intensity I and hydraulic diameter at the inlet cross section (intensity and hydraulic diameter), and the hydraulic diameter, D_H , was 30 mm.
Flow Reynolds number:

$$Re_{D_H} = \frac{\rho v_{in} D_H}{\mu} = \frac{1.93 \times 50 \times 0.03}{2.745 \times 10^{-5}} = 1.05 \times 10^5. \tag{11}$$

Turbulence Intensity:

$$I = 0.16(Re_{D_H})^{-\frac{1}{8}} = 0.16 \times (1.05 \times 10^6)^{-\frac{1}{8}} = 3.77\%. \tag{12}$$

2. Outlet: Pressure outlet. Pressure was set to 0 Pa.
3. Wall: The wall parameters were standard, and there was no slip condition.
4. Porous media: The viscous drag coefficient, inertial drag coefficient, and porosity of porous media were calculated using (13) and (14), where D_f is fiber diameter, ε_1 is the porosity, and C_4 , C_5 are constants

$$\alpha_1 = \frac{D_f^2 \varepsilon_1^3}{150(1 - \varepsilon_1)^2}, \tag{13}$$

$$C_4 = \frac{1}{\alpha_1}, \quad C_5 = \frac{3.5(1 - \varepsilon_1)}{D_f \varepsilon_1^3}. \tag{14}$$

We defined $D_f = 20 \mu\text{m}$ and $\varepsilon_1 = 0.92$, as mentioned in the literature [30]. Then, C_4 and C_5 were solved using Eq. (14), to be $3.08210734 \times 10^9 \text{ m}^{-2}$ and $17,978.95948 \text{ m}^{-1}$, respectively.

3.2.2 Gas–solid two-phase flow field

The boundary condition for the gas fluid was as noted in subsection 3.2.1, and the discrete phase model was used to simulate the gas–solid two-phase flow in the proposed separator. Particles were injected with the gas into the flow stream, normal to the separator inlet surface.

The high-temperature molten salt cooling experiment was carried out in the SIAP lab. In terms of sample analysis, particle size and corresponding mass fractions were measured, giving the results shown in Table 1.

The total mass fractions for the different particle size range were statistically calculated, as shown in Fig. 3. It should be noted that the corresponding mass fraction was for all particles larger than the referenced particle diameter.

According to the Rosin–Rammler equation [31], the solid particle distribution index is calculated using Eq. (15), where D_m represents the medium particle diameter, as $Y = 36.8\%$, and is defined as 1.13 μm , from Fig. 3.

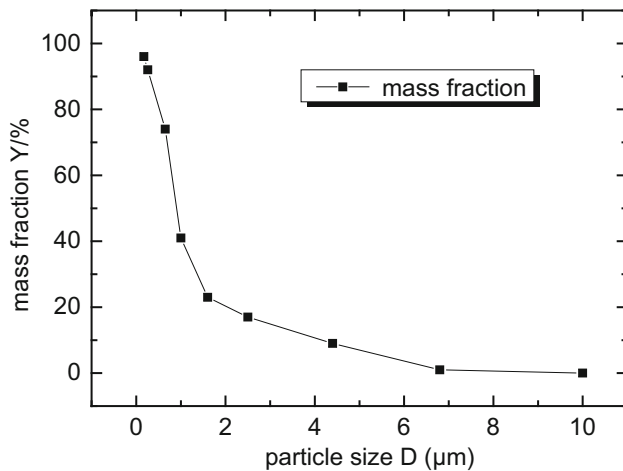
$$n = \text{AVERAGE} \left\{ \frac{\ln(-\ln Y(D_i))}{\ln\left(\frac{D_i}{D_m}\right)} \right\}_{i=1,2,\dots,8} \tag{15}$$

Using the inputs above, the distribution index was then calculated to be $n = 1.17$.

DPM boundary conditions were as follows:

Table 1 Nuclear waste gas sampling analyses

Particle diameter (D , μm)	0.17	0.26	0.65	1.0	1.6	2.5	4.4	6.8	10
Mass fraction (wt%)	4	4	18	33	18	6	8	8	1

**Fig. 3** Particle diameter fitting diagram

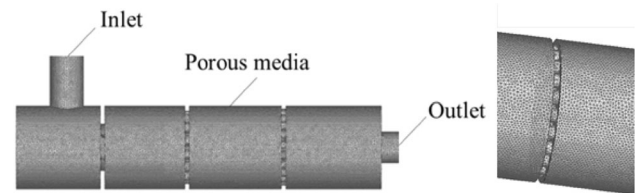
1. Inlet: Escape, indicating that particles could pass through this section.
2. Outlet: Escape, indicating that particles that were not separated, escaped.
3. Bottom wall: Trap, indicating that particles collected here.
4. Filter walls: Trap.
5. Other walls: Reflect.

3.3 Computational methodology

Fluid flow numerical simulations were obtained with computer code ANSYS 16.0, which is based on a finite volume technique, while the SIMPLE algorithm was used to solve the flow and pressure equations, and the standard method was employed in the pressure term. The second order, upwind algorithm mentioned in Ref. [32] was employed in simulating the boundary layer motion of the fluid. All of the governing equations were solved using the pressure-based, coupled algorithm. The residual for all equations was $< 10^{-3}$.

3.4 Mesh generating and grid independence verification

The accuracy of a CFD solution is strongly determined by the number and type of meshed elements within the computational domain [33, 34]. In order to obtain the best results, the whole model was divided into blocks, and a non-uniform, unstructured grid, using tetrahedrons as

**Fig. 4** Geometric meshing

elements, was employed, as shown in Fig. 4. The mesh in the blade and porous media regions was locally refined.

The grid independence test was performed, in order to ensure calculation accuracy; the calculations were therefore primarily carried out using five different grid sizes, with 1.15×10^6 , 1.64×10^6 , 2.82×10^6 , 3.11×10^6 , and 3.83×10^6 grids, respectively. The computational pressure drop deviation between each two adjacent grid sets was 1.42%, 1.27%, 0.86%, and 0.69%, respectively, which indicated that this CFD numerical model and method had high precision and was reasonable. After comprehensively considering calculation accuracy and efficiency, our final calculations were performed using the fourth grid set, that is, with grid number of 3.11×10^6 .

4 Model verification

The blade and the filter were the two key parts of the proposed combined separator. The filter was generally taken as porous media, and its flow field was simulated using a laminar model; however, the blade zone flow field needed to be studied using a turbulence model. In order to obtain accurate results, optimal selection of turbulent models should be conducted for the blade zone, by referring to experimental data in the literature [35].

The experimental cyclone structure was similar to the blade structure of the combined separator. The inlet pressure and temperature were 100,020 Pa and 19 °C, respectively. To decrease measuring error, experiments were repeated seven times, and the resultant data standardized. The maximum and minimum deviations were 11.6% and -3.59% , respectively. The final, standardized experimental results for the seven flow runs were published in Ref. [35], where the numerical axial cyclone separator dimensions were the same as that used in this experiment, except that, in order to make the fluid flow full; the inlet and outlet were extended by 100 mm and 840 mm, respectively. Four turbulent models were used to simulate the structure flow fields, as mentioned above, and the

numerical pressure drops obtained were compared with experimental results and are shown in Fig. 5.

Comparing the experimental pressure drops, as illustrated in Fig. 5, the deviation of the numerical results obtained using the standard k - ϵ model was the least—within $\pm 10\%$ —while the others' deviations were $> 10\%$. This indicated that the standard k - ϵ turbulence model and numerical calculation method were both appropriate and accurate.

5 Results and discussions

5.1 Velocity field

To understand detailed fluid flow information, velocity distributions at different cross sections, and for the whole separator, were investigated. Along the z -axis, 11 cross sections were investigated, as shown in Fig. 2. Z_1 – Z_5 were in the blade zone, from $Z = 0.091$ – 0.111 m, and each pair of adjacent cross sections was 5 mm apart. Cross sections Z_6 – Z_{11} were in the filter zone, and each pair of adjacent cross sections was 10 mm apart, from $Z = 0.174$ – 0.224 m. Path h' was defined along the y -axis direction, as the center line of each cross section.

Figure 6a shows the velocity magnitude contours of the new combined separator, on the longitudinal section of $y = 0$, and it can be seen that velocity changed faster in the blade zone, at the flower board, and at the outlet pipe, due to the changes in actual flow area. Velocity distribution in the filter zone was relatively uniform.

In order to understand the blade zone flow mechanism, velocity was investigated at five cross sections along the z -axis, and velocity distribution at cross sections Z_1 – Z_5 in the blade zone is shown in Fig. 6b–f, where it is apparent that

the velocity distribution differed over height. Along the z -axis, the maximum velocity magnitude and gradient increased with separator height, with the maximum velocity at cross section Z_1 being 49.8459 m/s, which increased to 112.037 m/s by Z_5 . In addition, the high-velocity areas at Z_1 and Z_2 were larger and decreased with increased height, while those at Z_3 – Z_5 were smaller and appeared in the corner near the inner cylinder. This phenomenon was caused by reduction in flow area, which was itself dependent on the blade layout.

Velocity contours for filter zone cross sections are shown in Fig. 7, where it can be seen that the velocities were almost centrosymmetric, and appeared relatively uniform for all of the cross sections.

Tangential velocity distribution along path h' in the cross sections is shown in Fig. 8, where it can be seen that in the blade zone, tangential velocity was antisymmetrically distributed along the radial direction. Due to blade influence, tangential velocity fluctuated, exhibiting rapid changes. The maximum tangential velocities for different cross sections occurred at different radii, and the greater the tangential velocity, the easier the gas–solid separation.

Tangential velocity along path h' was almost 0 in the filter zone, which implied that there was no swirling effect, and that gas–solid separation was carried out only by the filter.

5.2 Pressure field

Static pressure distributions on the longitudinal section are shown in Fig. 9a, where it can be seen that static pressure gradually decreased along the z -axis, while in the blade zone, static pressure increased in the radial direction. A low-pressure zone appeared in the center of the cyclone, due to its high swirling velocity, and it was apparent that the filter zone pressure gradient was very large, and almost constant in the radial direction.

Figure 9b–f shows static pressure contours for cross sections Z_1 – Z_5 in the blade zone, and indicates that the maximum static pressure at the cross sections decreased along the z -axis. The high-pressure area at Z_1 was smaller and increased with increasing height, while it was larger at Z_4 – Z_5 . It should be pointed out that the static pressure in six independent regions behind the blades decreased clockwise, in all cross sections.

Static pressure contours for filter zone cross sections are shown in Fig. 10, and it can be seen that cross-sectional static pressures at different heights were almost centrosymmetric, and were relatively uniform. Along the z -axis, maximum static pressure decreased with separator height, and thus, while the maximum static pressure at cross section Z_6 was 122,709 Pa, by Z_{11} it had decreased to 48,620 Pa.

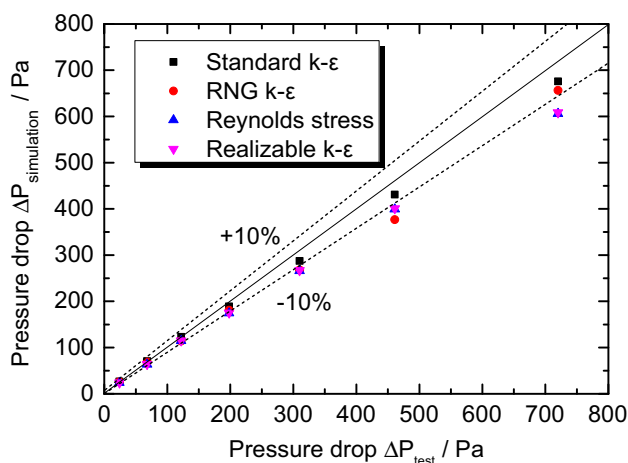


Fig. 5 Comparisons between experimental pressure drop and numerical results

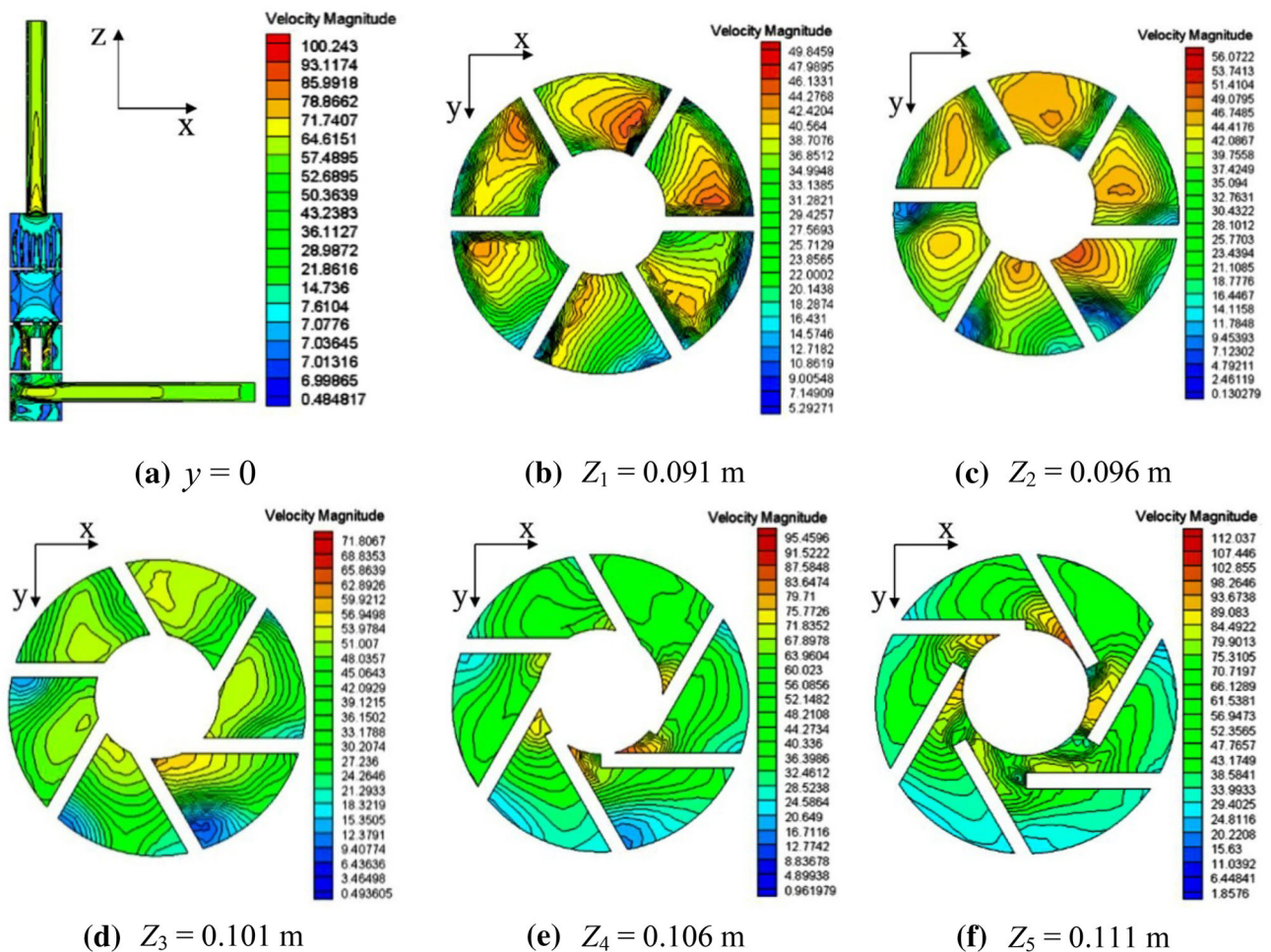


Fig. 6 (Color online) Velocity contours (m/s) at several cross sections

Static pressures along cross-sectional paths are shown in Fig. 11. In the blade zone, static pressure at different heights increased with increased radius, reaching its maximum near the cylinder wall. In the filter zone, static pressure varied significantly with separator height, while showing constant behavior radially, at any given height.

5.3 Particle trajectory and separation efficiency

Based on gas field flow, discrete phase particles were added, and their resultant trajectories are shown in Fig. 12.

From Fig. 12a, it can be seen that coarse particles were mainly concentrated in the settlement chamber, and then after this first-stage separation, particle concentration was reduced, and most of the unseparated particles escaped from the outlet. Ultimately, 720 particles were emitted, 147 were captured, 553 particles escaped, and the trajectories of 20 particles were incomplete. Based on these results, the separation efficiency, η_1 , of the combined separator—without filter material—was calculated to be 20.42%.

Particles were mostly captured after flowing through the new combined separator, as shown in Fig. 12b. Of the 720 particles emitted, 692 particles were captured and 28 particles were recorded as incomplete. Therefore, the combined separator—with filter material—showed that it could separate particles with 96.11% efficiency.

The tests showed that first-stage axial cyclone separation greatly influenced the combined separator's total efficiency. In summary, the higher the first-stage separation efficiency, the smaller the particles that were able to enter the second-stage filter which would result in reduced particle wear and maintenance costs.

6 Influence of structural parameters

Blade structure determines first-stage separation efficiency, so in order to obtain higher separation efficiency and reduced pressure drop, the influence of key blade structure parameters is needed to be studied.

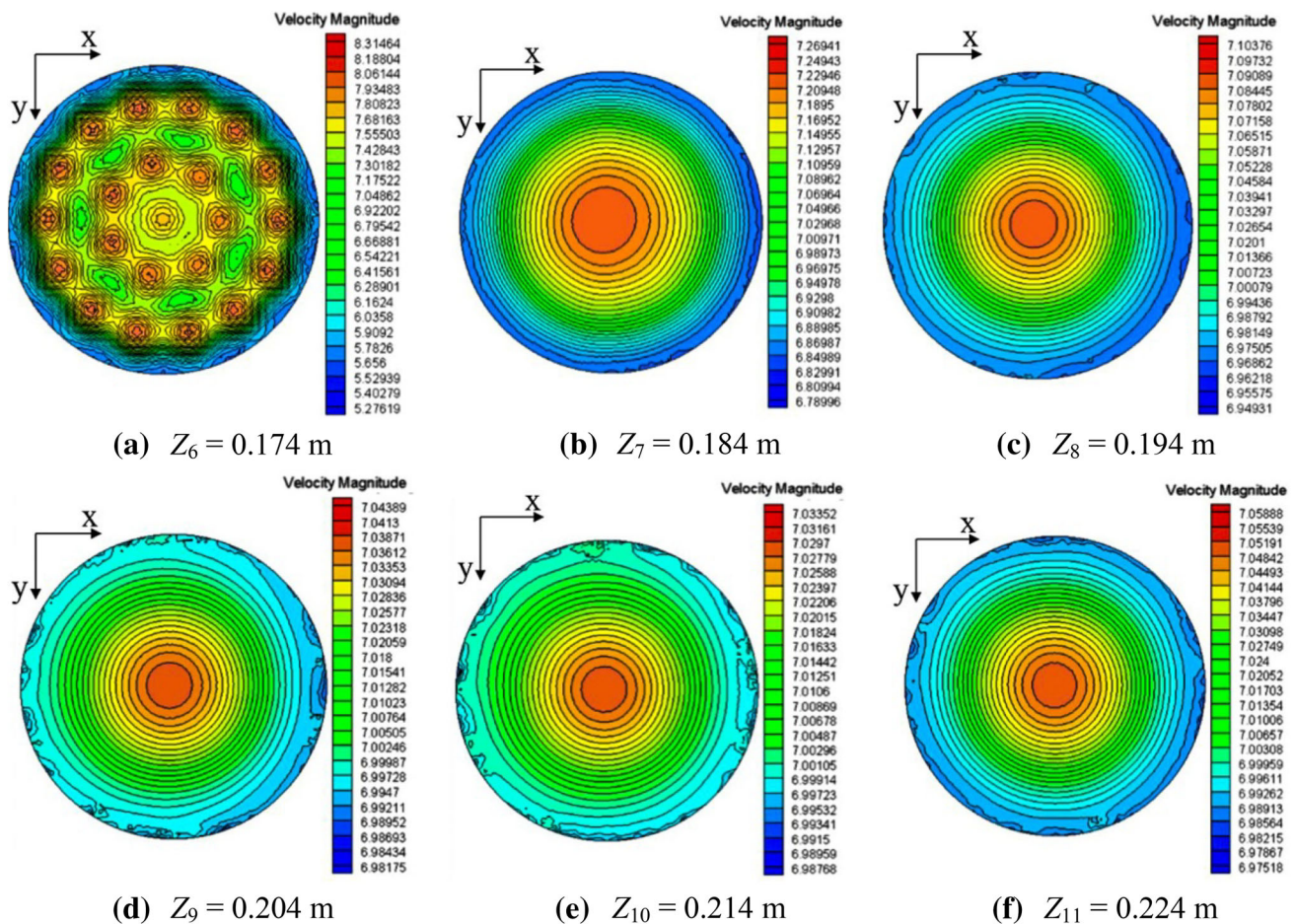


Fig. 7 (Color online) Velocity contours (m/s) for filter zone cross sections

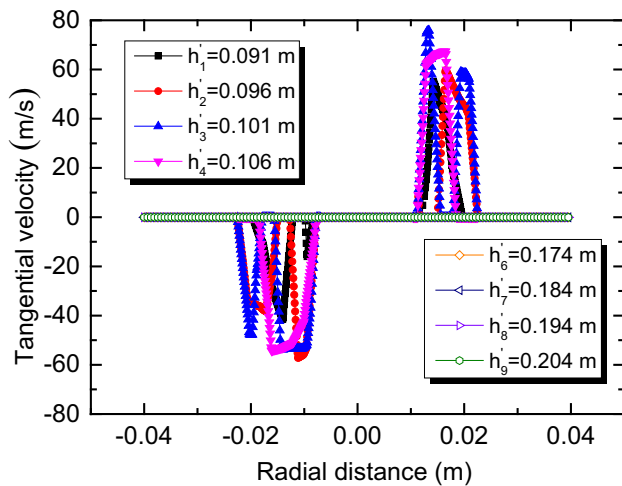


Fig. 8 (Color online) Tangential velocities along cross-sectional paths

6.1 Blade inclination angle

Considering the actual working conditions and due to installation and manufacturing limitations, generally, blade

inclination angles were between 15° and 60°. These limits occur as, firstly, since the blades overlap, they can be easily damaged when the blade inclination angle < 15°, while, secondly, if the angle > 60°, the fluid will flow in parallel fashion along the z-axis, thus decreasing gas–solid separation efficiency.

Using a six-bladed configuration, numerical studies were conducted on the separation performance of ten combined separators with different blade angles, and the resulting pressure drop and separation efficiency of these combined separators are shown in Fig. 13.

The combined separator pressure drop showed the same trend in variation with and without filter material, with pressure drop decreasing before becoming constant, with increased blade inclination angle. Blade inclination angle showed great effect on pressure drop when it was < 40°.

The separation efficiency of the combined separator—without filter material—fluctuated with blade inclination angle, reaching its maximum at 45°, but when filter material was introduced, the separation efficiency increased slightly at first, before decreasing with further inclination angle increase. When the blade inclination

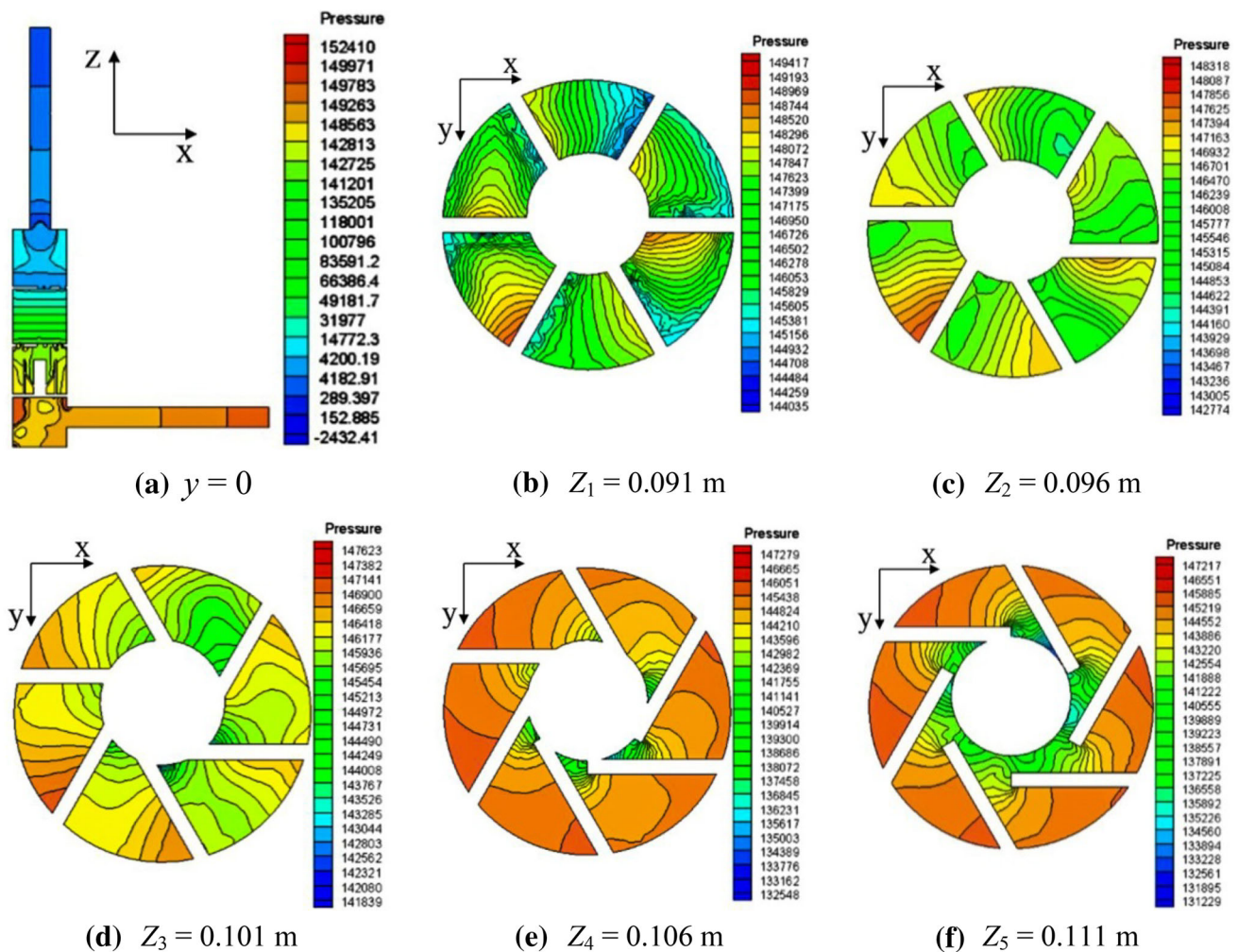


Fig. 9 (Color online) Cross-sectional static pressure contours (Pa)

angle was 45° , separation efficiency jumped to its maximum as the 45° blade inclination made gas–solid inertial separation and fluid flow relatively stable. Based on these results, it was settled that the optimum blade inclination angle was 45° .

6.2 Blade number

Using 45° blade inclination, numerical simulation of separators designed with a variety of blade numbers was conducted, and the resultant pressure drops and separation efficiencies are shown in Fig. 14.

From Fig. 14, the combined separator pressure drop—with or without filter material—shows the same variation trend. With increased blade number, pressure drop increased, with this effect increasing when the blade number $>$ six.

Separation efficiency fluctuated with blade number. For the combined separator without filter material, separation efficiency varied slightly with blade number, reaching a maximum of 30% with four blades. For the combined separator with filter material, the efficiency was constant, at $\sim 97\%$, before suddenly decreasing to $\sim 65\%$ when the blade number $>$ six. Separation efficiency was then further reduced when the blade number was $>$ seven, indicating overall that a four-bladed design was optimum.

For the optimized structure without filter material, pressure drop decreased, from 7.12 kPa to 6.66 kPa, while separation efficiency increased, from 20.42 to 29.45%. With filter material, the pressure drop decreased, from 144.13 to 143.95 kPa, while separation efficiency increased from 96.11 to 98.81%. Compared with the original design, separation efficiency per unit of pressure drop improved by 2.99% and 54%, for the optimum structure with or without filter material, respectively.

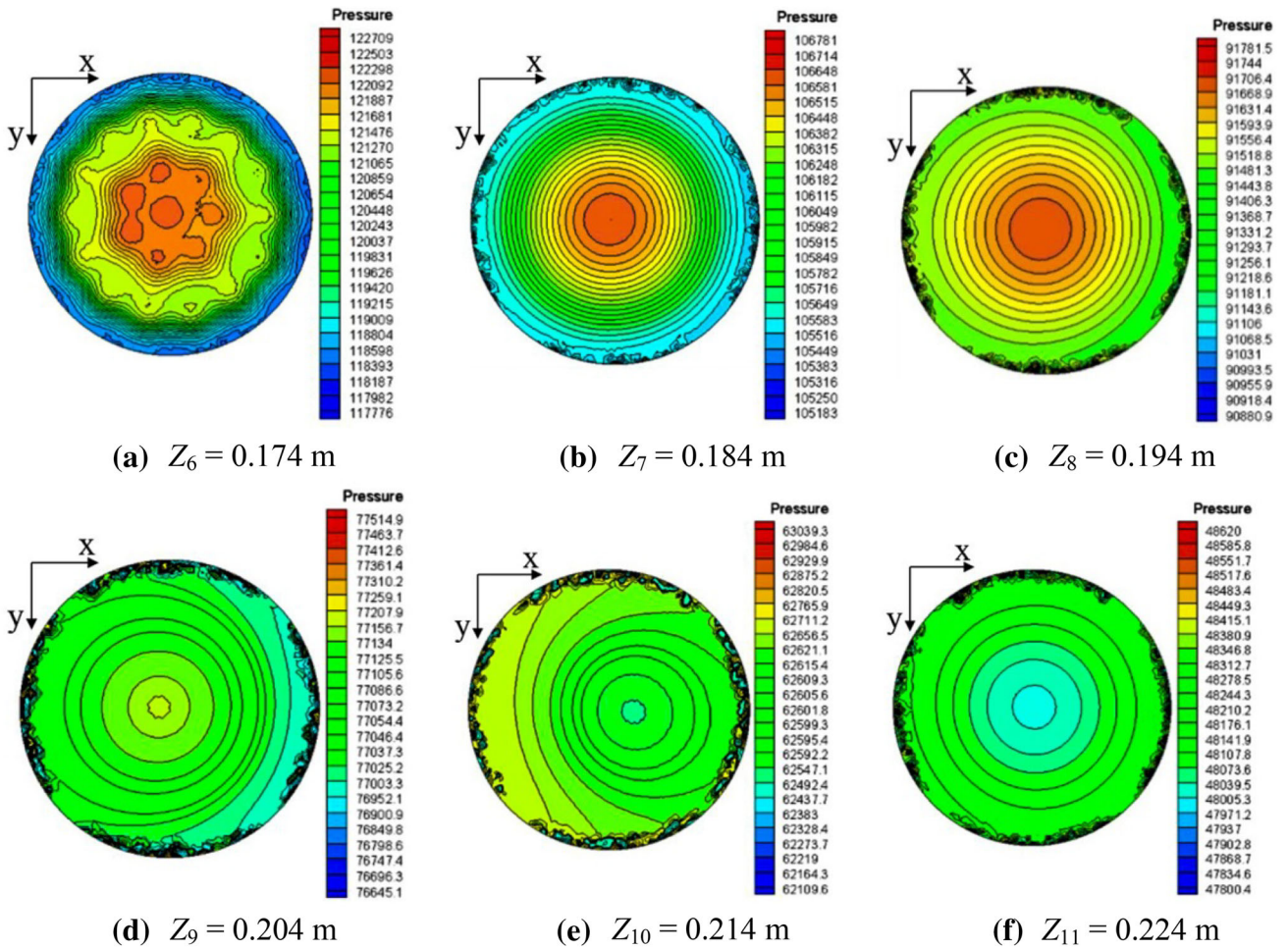


Fig. 10 (Color online) Filter zone cross-sectional static pressure contours (Pa)

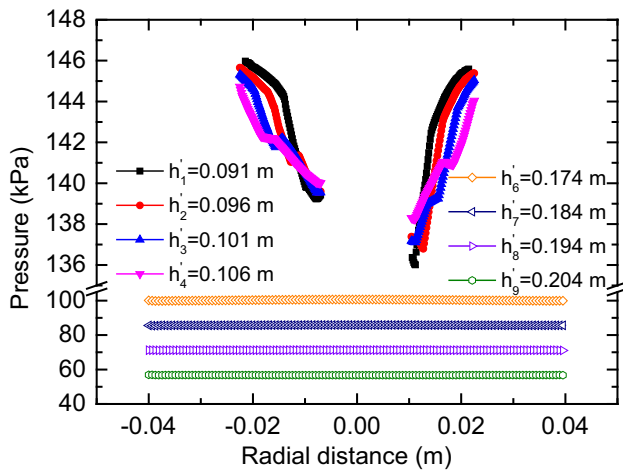


Fig. 11 (Color online) Static pressure along cross-sectional paths

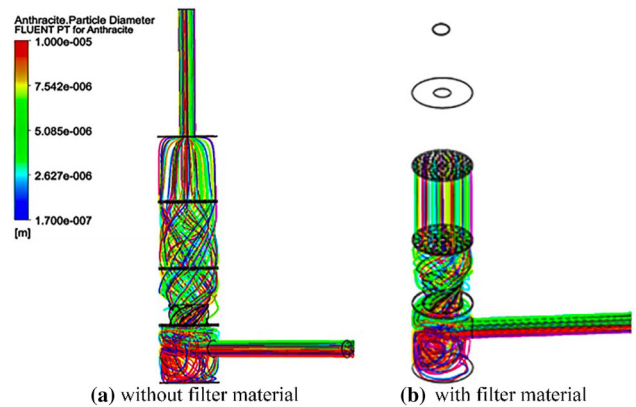


Fig. 12 (Color online) Particle trajectories in the combined separator

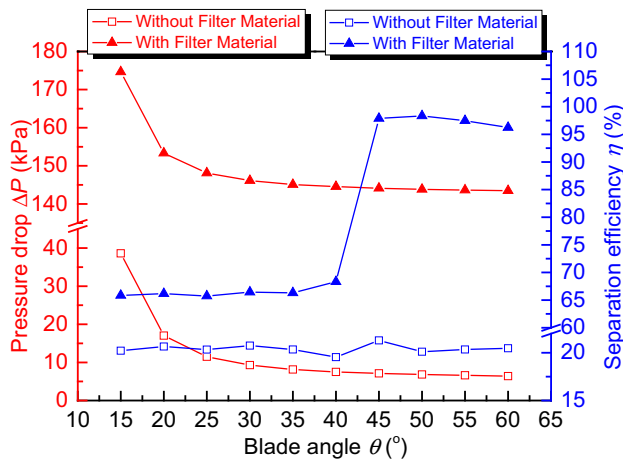


Fig. 13 (Color online) Effect of blade inclination angle on combined separator pressure drop and separation efficiency

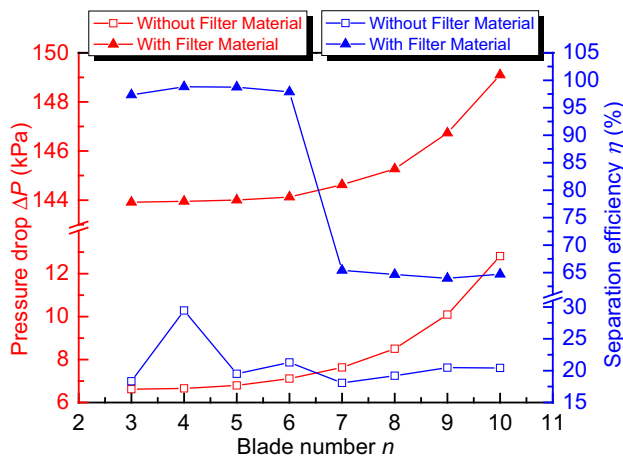


Fig. 14 (Color online) Effect of blade number on combined separator pressure drop and separation efficiency

7 Conclusions

In this study, a new combined separator, designed as exhaust removal equipment for a TMSR-SF, has been proposed. Gas–solid, two-phase flow fields were simulated, using CFD, and then the influence of key structural parameters on separation performance was analyzed. The following conclusions can be drawn from the study:

1. Using the experimental results, an accurate CFD numerical model and method for the new combined separator have been proposed.
2. In the blade zone, the maximum velocity magnitude and gradient increased with separator height (along the z -axis), while static pressure increased in the radial direction. A low-pressure zone appeared in the center of the cyclone, due to high swirling velocity, while in the filter zone, velocity distribution was relatively

uniform. Static pressure decreased along the z -axis, while being almost constant in the radial direction.

3. Combined separator gas–solid separation efficiencies, with and without filter material, were 96.11% and 20.42%, respectively, with first-stage axial cyclone separation showing significant influence on the combined separator's total efficiency.
4. With increased blade inclination angle, the combined separator pressure drop, with or without filter material, decreased, before becoming constant, while it increased with increased blade number. The separation efficiency of the combined separator with or without filter material fluctuated with blade inclination angle and number, and four blades, with a 45° inclination angle was determined to be the optimum combination for the new design. Separation efficiency per unit of pressure drop improved by 2.99% and 54%, for the optimum structure, with or without filter material, respectively.

References

1. J. Serp, M. Allibert, O. Benes, et al., The molten salt reactor (MSR) in generation IV: overview and perspectives. *Prog. Nucl. Energy* **77**, 308–319 (2014). <https://doi.org/10.1016/j.pnucene.2014.02.014>
2. C.Y. Zou, C.Z. Cai, C.G. Yu et al., Transition to thorium fuel cycle for TMSR. *Nucl. Eng. Des.* **330**, 420–428 (2018). <https://doi.org/10.1016/j.nucengdes.2018.01.033>
3. K.C. Sun, J. Wilson, S. Hauptman et al., Neutronics modeling and analysis of the TMSR-SF1 fuel lattice and full core with explicit fuel particle distribution and random pebble loadings. *Prog. Nucl. Energy* **109**, 171–179 (2018). <https://doi.org/10.1016/j.pnucene.2018.08.005>
4. H. Xu, Z. Dai, X. Cai, Some physical issues of the thorium molten salt reactor nuclear energy system. *Nucl. Phys. News* **24**(2), 24–30 (2014). <https://doi.org/10.1080/10619127.2014.910434>
5. T. Allen, S. Ball, E. Blandford, et al., *Preliminary Fluoride Salt-Cooled High Temperature Reactor (FHR) Subsystems Definition, Functional Requirement Definition and Licensing Basis Event (LBE) Identification White Paper* (University of California, Berkeley, 2012), p. 4
6. T. Allen, E. Blandford, G. Cao, et al., *Preliminary Fluoride Salt-Cooled High Temperature Reactor (FHR) Methods and Experiments Program White Paper* (University of California, Berkeley, 2012), p. 3
7. C. Forsberg, P.F. Peterson, Basis for fluoride salt-cooled high-temperature reactors with nuclear air-brayton combined cycles and firebrick resistance-heated energy storage. *Nucl. Technol.* **196**(1), 13–33 (2016). <https://doi.org/10.13182/NT16-28>
8. A.L. Qualls, B.R. Betzler, N.R. Brown et al., Preconceptual design of a fluoride high temperature salt-cooled engineering demonstration reactor: motivation and overview. *Ann. Nucl. Energy* **107**, 144–155 (2017). <https://doi.org/10.1016/j.anucene.2016.11.021>

9. M.H. Jiang, H.J. Xu, Z.M. Dai, Advanced fission energy program—TMSR nuclear energy system. *Bull Chin Acad Sci* **27**(3), 366–373 (2012). <https://doi.org/10.3969/j.issn.1000-3045.2012.03.016>. (in Chinese)
10. P.K. Romano, N.E. Horelik, B.R. Herman et al., Open MC: a state-of-the-art monte carlo code for research and development. *Ann. Nucl. Energy* **82**, 90–97 (2015). <https://doi.org/10.1016/j.anucene.2014.07.048>
11. R.M. Ji, Y. Dai, G.F. Zhu et al., Evaluation of the fraction of delayed photoneutrons for TMSR-SF1. *Nucl. Sci. Tech.* **28**(9), 135 (2017). <https://doi.org/10.1007/s41365-017-0285-9>
12. R.M. Ji, M.H. Li, Y. Zou, et al., Impact of photoneutrons on reactivity measurements for TMSR-SF1. *Nucl. Sci. Tech.* **28**, 76 (2017). <https://doi.org/10.1007/s41365-017-0234-7>
13. J. Zhou, S. Hao, L. Gao et al., Study on adsorption performance of coal based activated carbon to radioactive iodine and stable iodine. *Ann. Nucl. Energy* **72**, 237–241 (2014). <https://doi.org/10.1016/j.anucene.2014.05.028>
14. J.R. Zhang, J.R. Hou, D.P. Shen et al., Indigenization re-search of activated carbon adsorbent for radioiodine waste gas treatment system at a nuclear plant. *Radiat. Prot.* **33**(5), 38–40 (2013). <https://doi.org/10.3969/j.issn.1004-6356.2013.05.008>. (in Chinese)
15. H. Safikhani, P. Mehrabian, Numerical study of flow field in new cyclone separators. *Adv. Powder Technol.* **27**(2), 379–387 (2016). <https://doi.org/10.1016/j.appt.2016.01.011>
16. S.G. Bogodage, A.Y.T. Leung, CFD simulation of cyclone separators to reduce air pollution. *Powder Technol.* **286**, 488–506 (2015). <https://doi.org/10.1016/j.powtec.2015.08.023>
17. Q.P. Li, J. Xie, Y.J. Xu, et al., A combined dust collector for combustible gas. China. Patent 201510657221. 12 Oct 2015
18. P. Tronville, R. Sala, Minimization of resistance in pleated-media air filter designs: empirical and CFD approaches. *HVAC&R Res.* **9**(1), 95–106 (2003). <https://doi.org/10.1080/10789669.2003.10391058>
19. M.Y. Hu, K. Che, J. Zhang et al., Numerical simulation of air distribution in the series-type electrostatic fabric filter precipitator. *Adv. Mater. Res.* **383–390**, 6530–6536 (2011). <https://doi.org/10.4028/www.scientific.net/AMR.383-390.6530>
20. L.X. Zhou, S.L. Soo, Gas–solid flow and collection of solids in a cyclone separator. *Powder. Technol.* **63**(1), 45–53 (1990). [https://doi.org/10.1016/0032-5910\(90\)80006-k](https://doi.org/10.1016/0032-5910(90)80006-k)
21. J.Y. Tian, R.F. Tian, L.X. Sun, et al., Numerical study of characteristic of an axial flow cyclone. *Prog. Rep. China Nucl. Sci. Technol.* **3**, 658–663 (2013)
22. M. Azadi, M. Azadi, A. Mohebbi, A CFD study of the effect of cyclone size on its performance parameters. *J. Hazard. Mater.* **182**(1–3), 835–841 (2010). <https://doi.org/10.1016/j.jhazmat.2010.06.115>
23. M.A.M. Nor, H.H. Al-Kayiem, T.A. Lemma, Numerical analysis of cocurrent conical and cylindrical axial cyclone separators. *IOP Conf. Ser. Mater. Sci. Eng.* **100**, 012054 (2015). <https://doi.org/10.1088/1757-899x/100/1/012054>
24. M. Wasilewski, Analysis of the effect of counter-cone location on cyclone separator efficiency. *Sep. Purif. Technol.* **179**, 236–247 (2017). <https://doi.org/10.1016/j.seppur.2017.02.012>
25. B. Zhao, Y. Su, J. Zhang, Simulation of gas flow pattern and separation efficiency in cyclone with conventional single and spiral double inlet configuration. *Chem. Eng. Res. Des.* **84**(12), 1158–1165 (2006). <https://doi.org/10.1205/cherd06040>
26. Y.G. Luan, H.O. Sun, Effect of blade numbers on pressure drop of axial cyclone separators by CFD. *Appl. Mech. Mater.* **55–57**, 343–347 (2011). <https://doi.org/10.4028/www.scientific.net/AMM.55-57.343>
27. J. Zhao, Q.Q. Zhu, D.S. Fan, Numerical simulation on fiber ball filter for porous media model. *Chem. Eng. Mach.* **39**(3), 343–346 (2012). <https://doi.org/10.3969/j.issn.0254-6094.2012.03.022>. (in Chinese)
28. ANSYS Inc., *ANSYS FLUENT 12.0 Theory Guide* (Canonsburg, USA, 2009)
29. S.A. Morsi, An investigation of particle trajectories in two-phase flow systems. *J. Fluid Mech.* **55**, 193–208 (1972). <https://doi.org/10.1017/S0022112072001806>
30. B. Ding, Y.Y. Li, X.L. Zhao, et al., Electret nano-fiber air filtering material with waterproof function and preparation method therefore. China. Patent 201611270720. 31 May 2017
31. B. Wang, D.L. Xu, K.W. Chu, et al., Numerical study of gas–solid flow in a cyclone separator. *Appl. Math. Model.* **30**(11), 1326–1342 (2006). <https://doi.org/10.1016/j.apm.2006.03.011>
32. T. Nie, Z.B. Wang, Y.H. Jin, Influence of guide vanes on the inner flow field in guide vane hydroclones. *Chem. Eng. Mach.* **35**(4), 224–227 (2008). <https://doi.org/10.3969/j.issn.0254-6094.2008.04.008>. (in Chinese)
33. H.K. Versteeg, W. Malalasekera, *An introduction to computational fluid dynamics, the finite method* (Wiley, Hoboken, 1995)
34. J.Y. Tu, G. Yeoh, C. Liu, *Computational fluid dynamics, a practical approach* (Elsevier, Berkeley, 2013)
35. Y.G. Luan, Numerical simulation and experimental study of axial flow cyclone separator. Harbin Engineering University, 2011. <https://doi.org/10.7666/d.y2053185>. (in Chinese)